$\mathcal{PT}$-symmetry-protected Dirac states in strain-induced hidden MoS_2 monolayer

Meiling Xu,[1,2] Guohui Zhan,[3,4] Siyu Liu,[2] Dongqin Zhang,[5] Xin Zhong,[6] Ziyang Qu,[1] Yinwei Li,[1,*] Aijun Du,[7] Haijun Zhang,[3,4,†] and Yanchao Wang[2,‡]

[1]*Laboratory of Quantum Materials Design and Application, School of Physics and Electronic Engineering, Jiangsu Normal University, Xuzhou 221116, China*

[2]*State Key Laboratory of Superhard Materials & Innovation Center for Computational Physics Methods and Software, College of Physics, Jilin University, Changchun 130012, China*

[3]*National Laboratory of Solid State Microstructures, School of Physics, Nanjing University, Nanjing 210093, China*

[4]*Collaborative Innovation Center of Advanced Microstructures, Nanjing University, Nanjing 210093, China*

[5]*Department of Physics, China Jiliang University, Hangzhou, Zhejiang 310018, People's Republic of China*

[6]*Key Laboratory of Functional Materials Physics and Chemistry of the Ministry of Education, Jilin Normal University, Changchun 130103, China*

[7]*School of Chemistry, Physics and Mechanical Engineering, Queensland University of Technology, Gardens Point Campus, Brisbane QLD 4001, Australia*

(Received 31 October 2019; published 19 December 2019)

Two-dimensional (2D) materials have recently attracted significant interest in condensed-matter physics and materials science due to rich intriguing physics and potential applications. Here, by first-principles calculations, we discover a phase of transition-metal dichalcogenides (MoS_2 and its family) named the $1H'$ phase. We demonstrate that $1H'$ MoS_2 monolayer has multiple topological phase transitions from a topologically trivial insulator state to a 2D type-II Dirac semimetal state, and then to a 2D ideal type-I semimetal state under a moderate tensile strain. The Dirac points are protected by the coexistence of space-inversion (P) and time-reversal (T) symmetry. Our results highlight a family of nonhoneycomb 2D Dirac semimetals with potential application in nanoelectronics.

DOI: 10.1103/PhysRevB.100.235435

I. INTRODUCTION

Topological semimetals, such as Weyl/Dirac semimetals, can host rich exotic physical phenomena, and they have attracted widespread attention in condensed-matter physics and materials science [1–3]. So far, many typical topological semimetals have been discovered for the three-dimensional (3D) case, e.g., the TaAs family as Weyl semimetals [4–9], the $MoTe_2$ family as type-II Weyl semimetals [10–12], the HgTe family as ideal Weyl semimetals [13,14], and Na_3Bi and Cd_3As_2 as Dirac semimetals [15–21]. Experimentally, gapless linear dispersions, topologically protected surface states with a Fermi arc, and negative magnetoresistance induced by the chiral anomaly have been successively observed [7,22–25]. For the two-dimensional (2D) case, the Weyl/Dirac semimetallic states could also exist [26–28], but the external symmetries are necessary to protect gapless Weyl/Dirac points. The representative example of 2D Dirac semimetals is currently limited to graphene with two Dirac cones at K and K' points in the Brillouin zone [28]. In recent years in the study of 2D materials, significant progress has been made on the experimental synthesis of many new monolayers of 2D materials, such as silicene, germanene, stanene, black phosphorus and transition-metal dichalcogenides (TMDs) [29–34]. Interestingly, topological states were also discovered in TMD materials, e.g., the quantum spin Hall state in $1T'$ WTe_2 monolayer [35] and the type-II Weyl semimetal state in T_d $MoTe_2$ [11,12,36,37]. This raises an interesting question on whether topological semimetals could exist in 2D material monolayers.

In this work, we have carried out the swarm-intelligence-based CALYPSO structure searches of TMD monolayer. We discovered a phase of MoS_2 monolayer and its family, denoted as $1H'$ phase with zigzag Mo-Mo chains from the side view, which is energetically more stable than the $1T$ phase. Moreover, moderate external tensile strains could lead to the formation of a rich phase diagram for $1H'$ MoS_2 and its family, including a topologically trivial insulator state and 2D type-II/ideal Dirac semimetal states. In the following, the $1H'$ MoS_2 monolayer will be used as an example to illustrate the electronic structure.

II. COMPUTATIONAL METHODS

Structure searches were carried out in simulation cells of up to 18 atoms using the swarm-intelligence-based CALYPSO method [38,39]. First-principles calculations were based on the density functional theory (DFT) [40] as implemented in the Vienna *ab initio* simulations package (VASP) [41]. The external potential was based on the

*Author to whom all correspondence should be addressed. yinwei_li@jsnu.edu.cn

†zhanghj@nju.edu.cn

‡wyc@calypso.cn

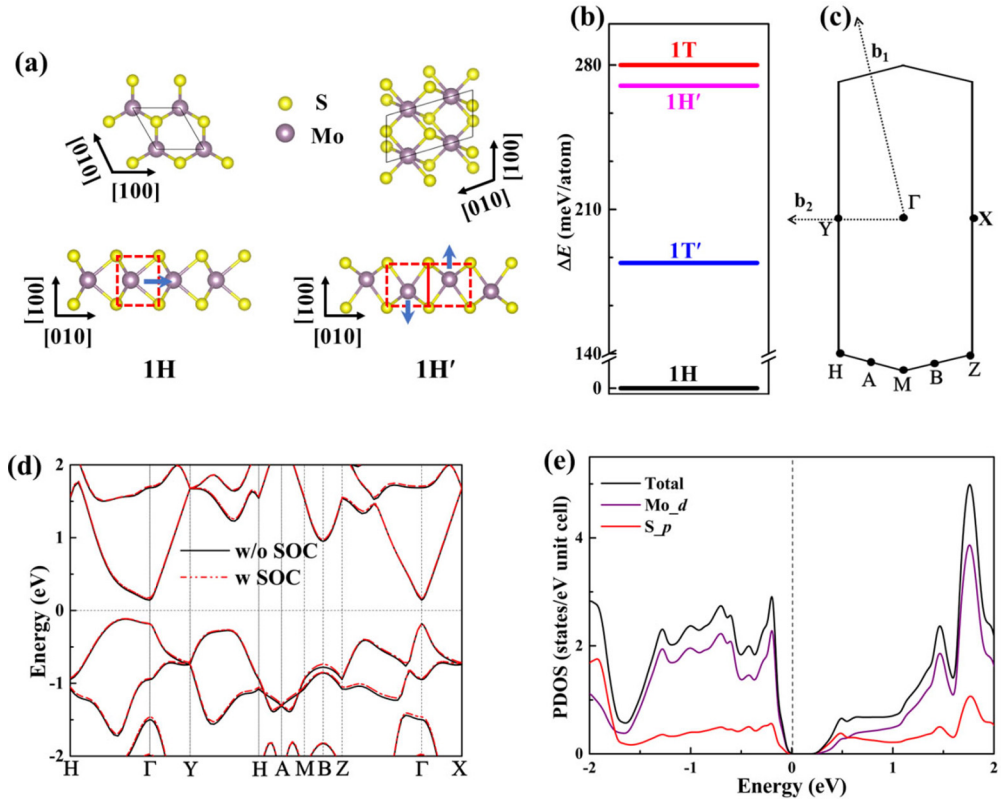

FIG. 1. (a) Top and side views of the crystal structure of 1H and 1H' MoS_2. The yellow and light purple spheres represent the S and Mo atoms, respectively. (b) Total energy of MoS_2 with different phases relative to 1H- MoS_2. (c) 2D Brillouin zones of 1H' MoS_2. (d) Band structures of 1H' MoS_2 at the HSE level with and without SOC. (d) The projected DOS of 1H' MoS_2 at the HSE level. The Fermi level is set to zero.

projector-augmented-wave (PAW) approximation [42] with the exchange-correlation functional in the generalized gradient approximation parametrized by Perdew, Burke, and Ernzerhof (GGA-PBE) [43]. The plane-wave cutoff energy was set to be 600 eV in all first-principles calculations, and the first Brillouin zone (BZ) was sampled using a 11 × 2 × 6 Monkhorst-Pack grid [44]. All the geometries were fully relaxed until residual forces are smaller than 10^{-3} eV/Å. Sufficient vacuum thickness (∼20 Å) was used along the y direction (i.e., perpendicular to the 2D sheet) to avoid spurious interaction among the periodic images. The dynamical stability was verified from phonon calculations using the direct supercell method (6 × 2 supercells) as implemented in the PHONOPY code [45,46]. To confirm the thermal stability, *ab initio* molecular-dynamics (AIMD) simulations were carried out for 6 ps with a time step of 1 fs. The temperature was controlled at 300–1800 K with an interval of 300 K using the Nosé-Hoover chain thermostat within 12 × 2 supercells containing 144 atoms. The Heyd-Scuseria-Ernzerhof (HSE) hybrid functional [47] was employed to get an accurate band gap. The edge states were obtained from the surface Green's functions of the semi-infinite system [48].

III. RESULTS AND DISCUSSIONS

By using the CALYPSO method, we successfully predicted all the known phases of MoS_2 monolayer including 1H, 1T, and 1T' phases, indicating the high reliability of the methodology. Interestingly, our unbiased structural searches also identified a low-lying phase, denoted as 1H' phase, containing six atoms per unit cell, as shown in Fig. 1(a). Similar to the well-studied 1H phase, the 1H' phase can also be viewed as a sandwich-type stacking of Mo and S atoms, wherein the layer of Mo atoms is sandwiched between two layers of S atoms and each Mo atom is coordinated to six S atoms. The optimized lattice parameters of the 1H' phase are $a = 3.09$ Å and $b = 5.96$ Å, respectively. Compared with the PBEsol functional, we found that the lattice constants of TMDs are larger by ∼1−2% using the PBE functional (Table SI of the supplemental material [49]). The total energies for different phases of MoS_2 are presented in Fig. 1(b) and Table SII [49], where all the total energies are relative to that of the 1H phase. Clearly, the 1H' phase is energetically more favorable than the 1T phase, suggesting it is highly possible for future experimental realization. Akin to the 1H phase, the structure unit (marked as a red dotted box) within the 1H' phase is also octahedral. The major difference is that the octahedral structure unit in the 1H' phase first rotates 90° clockwise and counterclockwise, and then is stitched together along the [010] direction (shown by arrows). The dynamical stability of the 1H' phase was verified by the phonon calculation as shown in Fig. S1 of the supplemental material [49]. The *ab initio* molecular-dynamics simulations have been carried out to evaluate thermal stability as shown in Fig. S2 [49]. Remarkably, the 1H' phase can withstand temperature as high as 1500 K without any structural destruction (Fig. S2 [49]). Considering the fact that the 1T

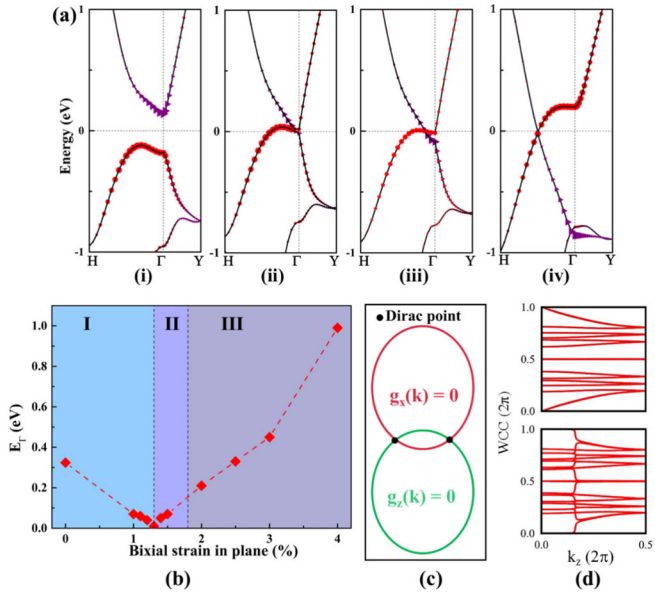

FIG. 2. (a) Orbital-resolved band structures under different strains: (i) 0%, (ii) 1.3%, (iii) 1.5%, and (iv) 4%. The red dots and purple triangles represent the contributions from the dz^2-orbitals of Mo atoms and p_y-orbitals of S atoms, respectively. (b) Band gap at Γ point as a function of biaxial strain. Different states are distributed in different regions. Regions I, II, and III represent an insulator state, a type-II Dirac semimetal state, and a type-I Dirac semimetal state, respectively. (c) Schematic diagram of the gapless point k_0 appears in the BZ. (d) The Wannier charge centers (WCCs) at strain of 0% and 4%.

MoS_2 has been experimentally realized, it is optimistic to synthesize the $1H'$ MoS_2 in experiments.

Figure 1(d) presents the calculated band structures for the $1H'$ MoS_2 monolayer at the HSE06 level. $1H'$ MoS_2 is semiconducting with an indirect band gap of ∼0.27 eV and the direct band gap at the Γ point is ∼0.32 eV. A comparison of the band structures as calculated with the HSE06 functional shows that the band gaps calculated are slightly large using the PBEsol (Fig. S3 [49]), but the conclusion of the topological property remains unchanged. It is worth noting that the band structure remains nearly unchanged when the spin-orbit coupling (SOC) is considered, indicating that the SOC effect is very weak in $1H'$ MoS_2. In $1H$ MoS_2, the broken inversion symmetry P enhances the spin orbital splitting and gives obvious spin splitting. Differently, the inversion symmetry P in $1H'$ TMDs is preserved, and the tiny intrinsic SOC effect dominates the band structure, so the SOC effect of $1H'$ TMDs seems very small. Therefore, the SOC effect is ignored in the following calculations unless it is specially stated. From the projected density of states (PDOS), shown in Fig. 1(e), we can see that the valence-band maximum (VBM) is mainly contributed by $4d$-orbitals of Mo atoms, while the conduction-band minimum (CBM) is dominated by $3p$-orbitals of S atoms. The similar d-p orbital characters are also observed in $1T'$ and $1T''$ MoS_2 [35,50]. Closer inspection of the orbital-resolved band structures [shown in Fig. 2(a)(i)] indicated that the VBM and CBM mainly consist of a d_{z^2} orbital of Mo atoms and a p_y orbital of S atoms, respectively.

The uniaxial/biaxial strain has been widely used to modulate the electronic structure of materials [13,51,52]. Experimentally, uniaxial/biaxial strains are often spontaneously induced due to the lattice mismatch during the growth of 2D material on substrates. To explore the effect of strain, biaxial tensile strains are gradually introduced in $1H'$ MoS_2 monolayer. Interestingly, the energy gap at the Γ point, between the VBM and the CBM, first started to reduce and then closed with increasing strain, as shown in Fig. 2a(ii). By further increasing the strain up to 1.5%, the energy gap at the Γ point reopens, indicating a band inversion. However, the band structure remains closed with band-crossing points along the Γ-H line, as shown in Fig. 2(a)(iii). As the SOC effect is ignored, the band crossing point is twofold-degenerate, known as a 2D Dirac point. Interestingly, the dispersion near the Dirac point is significantly tilted with both a hole and an electron Fermi pocket. The titled 2D Dirac point can be referred to as a type-II Dirac point, which is similar to a type-II Dirac point in the 3D case [53–55]. When the strain is further increased, the hole and electron Fermi pockets disappear, and the type-II Dirac point becomes an ideal 2D type-I Dirac point with the Dirac point exactly at the Fermi level, as shown in Fig. 2(a)(iv). Under tensile strain, the $1H'$ MoS_2 monolayer can have rich phase transitions from an insulator state to a type-II Dirac semimetal state and then to a type-I Dirac semimetal state as summarized in Fig. 2(b). We have explored the effect of uniaxial strain on topological states of $1H'$ MoS_2. The results demonstrate that the energy gap at the Γ point first started to reduce and then closed with increasing strain, as shown in Figs. S4 and S5 [49]. By further increasing the strain up to 1.5%, the energy gap at the Γ point reopens, indicating a band inversion. In other words, the uniaxial strain induces the same effect and phase diagram for $1H'$ MoS_2, including an insulator state, a type-II Dirac semimetal state, and a type-I Dirac semimetal state. Here, it is worth mentioning that uniaxial compressive tensile strain instead of uniaxial tensile strain is easy to apply experimentally, which is equal to biaxial tensile strain. Biaxial strain, as we know, can be easily obtained on a proper substrate.

Next, we turn to an investigation of the electronic structure of the 2D Dirac semimetallic states. As alluded to above, the tensile strain induced a band inversion between the valence and conduction bands, whose physical picture could be caught by a general two-band Hamiltonian $H(\mathbf{k})$,

$$H(\mathbf{k}) = \sum_{i=0,x,y,z} g_i(k)\sigma_i$$
$$= g_0(k) + g_x(k)\sigma_x + g_y(k)\sigma_y + g_z(k)\sigma_z,$$

where $k = (k_x, k_y)$, $g_{0,x,y,z}(k)$ are functions of k, σ_0 is a unit matrix, and $\sigma_{x,y,z}$ are Pauli matrices. In $1H'$ MoS_2 monolayer, the coexistence of inversion symmetry P and time-reversal symmetry T requires Hamiltonian $H(k)$ to be real [56], which leads to $g_y(k) = 0$ and $g_{x,z}(k)$ being real functions. The eigenvalue is $E(k) = g_0(k) \pm \sqrt{g_x(k)^2 + g_z(k)^2}$. If the gapless point k_0 appears, we inevitably have $g_x(k_0) = 0$ and $g_z(k_0) = 0$, which actually give two loops with intersections in the BZ from the geometric viewpoint, schematically shown in Fig. 2(c). The intersections have to be created and annihilated in pairs, which indicates a kind of topological stability. In

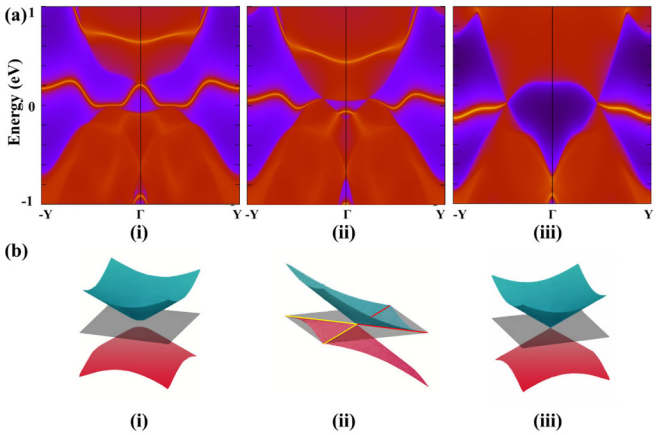

FIG. 3. (a) Edge states of $1H'$-MoS_2 at strains of (i) 0%, (ii) 1.8%, and (iii) 4.0% without SOC in the HSE level. (b) Schematic diagram of (i) an insulator, (ii) a type-II Dirac semimetal, and (iii) a type-I Dirac semimetal. The gray plane corresponds to the position of the Fermi level, and the yellow (red) lines mark the boundaries of the hole (electron) pockets.

fact, the intersections are merely Dirac points. Based on our calculations, we really find two Dirac points on the Γ-H lines in the BZ, shown in Fig. 2(a)(iii) and (iv). When it is close to the band inversion point, the Dirac points is seriously tilted to have both hole and electron pockets at the Fermi level, called 2D type-II Dirac semimetal. When the strain is further increased, the hole and electron Fermi pockets disappear and the 2D type-II Dirac semimetal becomes an ideal 2D Dirac semimetal with zero DOS at the Fermi level. Similar to that of graphene, two ideal 2D Dirac points in the $1H'$ MoS_2 are in the BZ, protected by the coexistence of P and T symmetries. The effective velocity of the Dirac points is calculated to be around 1.37×10^6 m/s, which is even larger than that of graphene, suggesting $1H'$ MoS_2 can have great potential applications in high-speed electronic devices. Different from graphene, the positions of Dirac points are not at K and K' but on Γ-H lines and the lattice of $1H'$ MoS_2 monolayer is not a honeycomb lattice. Additionally, the above rich phase diagram of $1H'$ MoS_2 can be simply tuned by an external strain.

The essential part of obtaining the Dirac points is the band inversion between p-orbitals of S atoms and d-orbitals of Mo atoms. The fat bands under different tensile strains are shown in Fig. 2(a). Without the strain, $1H'$ MoS_2 monolayer is insulating with a p-orbital characterized VBM and a d-orbital characterized CBM. With increasing strain, the energy gap closes at the Γ point and the band inversion happens between the VBM and the CBM, which leads to a topological transition. The Wannier charge centers, shown in Fig. 2(d), indicate that $1H'$ MoS_2 monolayer is initially a topologically trivial insulator, and then becomes topologically nontrivial after the band inversion. The external strain has an influence on spin-orbit splitting of bands of monolayer TMDs, especially at K and K' points [57]. Thus, it is reasonable to believe that the spin-orbit gap depends on strain. When the SOC effect is considered, the Dirac points open energy gaps of ∼6 and 11 meV at a strain of 1.5% and 4%. The tiny energy gap further confirms the weak SOC effect.

The existence of robust edge states is an important manifestation of a topological system. We then calculated the edge states for different phases of $1H'$ MoS_2 monolayers, shown in Fig. 3. For the topologically trivial insulator phase [see Fig. 3(a)(i)], there is a full energy gap for the bulk states and an edge state in the energy gap. This edge state is topologically trivial and is attributed to the specific dangling bonds. For the type-II Dirac semimetallic phase, the bulk states are gapless without a full energy gap and there are hole and electron Fermi pockets within the Dirac point. As expected, an edge state appears and robustly connects the Dirac points, seen in Fig. 3(a)(ii). For the ideal Dirac semimetallic phase, the hole and electron Fermi pockets disappear and the Dirac points are exactly located at the Fermi level. The edge state remains robust due to its topological origin, seen in Fig. 3(a)(iii). To investigate the stability of the topological edge state, the open boundary of $1H'$ MoS_2 monolayer is passivated with H atoms adsorbed at S, Mo, and Mo/S edges as schematically shown in Fig. 4. In our calculations, ${}^{4/3}H/{}^{2/3}H$ are used to passivate Mo/S dangling bands, respectively. As a hybrid functional is too computationally demanding, here the standard PBE functional is employed. We have confirmed that there is no essential difference for the case without absorbed H, seen in Figs. S6–S8 [49]. After saturating with H atoms, no extra edge states emerge and the edge state stays stable with different terminations. Interestingly, we notice that the edge state seems quite flat with a large effective mass over a large range of k-space. Such a flat edge state of 2D material is expected to

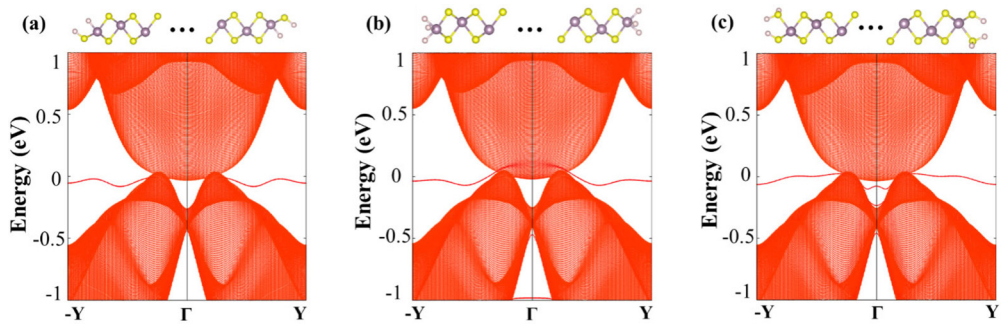

FIG. 4. Influence of different terminations on the edge states of $1H'$-MoS_2 under strain 4%. (a)–(c) The different termination and its hydrogen adsorption of $1H'$-MoS_2 nanoribbons are provided, where the yellow, light purple, and pink spheres represent the S, Mo, and H atoms, respectively. The band structures of $1H'$-MoS_2 nanoribbons with different terminations are calculated in the PBE level.

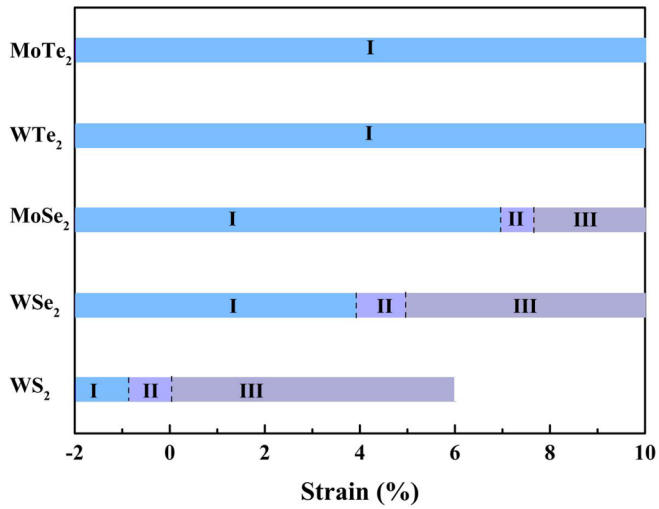

FIG. 5. The phase diagram of five other $1H'$ TMD monolayers induced by tensile strains we considered in this work. Regions I, II, and III represent an insulator state, a type-II Dirac semimetal state, and a type-I Dirac semimetal state, respectively.

provide a new platform to study strongly correlated many-body physics, such as magnetism and a fractional quantum Hall state.

Recent experiments have demonstrated that a reversible phase transition from $1H$ to other metastable phases in single- and few-layer MoS_2 structures can be achieved by electric doping [58,59]. To evaluate the effects of electron filling on the phase stability, we constructed a model system in which all Mo atoms are replaced by electron-richer Tc or Ru atoms. It is found that the $1H'$ phase of RuS_2 is energetically more favorable than the corresponding $1H$ phase (see Fig. S9 [49]), suggesting that the $1H'$ phase of MoS_2 may be obtained by adding two extra electrons per MoS_2.

$1T'$ MoS_2 monolayer with the quantum spin Hall effect was predicted by first-principles calculations, which was already verified in $1T'$ WTe_2 monolayer. Therefore, the $1H'$ phase may be observed experimentaly in other TMD monolayers, including $MoSe_2$, $MoTe_2$, WS_2, WSe_2, and WTe_2. As shown in Table SI [49], $1H'$ phases are energetically more favorable than the $1T$ phases for all these TMDCs. The calculated phonon-dispersion curves (see Fig. S10 [49]) conform that all the $1H'$ phases are dynamically stable. The corresponding band structures calculated at the PBE level are shown in Figs. S11–S16 [49]. Clearly, $1H'$ WS_2 monolayer is topologically nontrivial even in the absence of an external strain. It is worth noticing that the band inversion happens at the Γ point even when the SOC is not considered (see Fig. S17 [49]), which indicates that the topological property of $1H'$ WS_2 does not originate from the SOC effect. We think that the reason why $1H'$ WS_2 is topologically nontrivial in the absence of external strain should be more delocalized $5d$ orbitals of W atoms than $4d$ orbitals of Mo atoms. To test this idea, we adopt the virtual crystal approximation to calculate the band structures of $1H'$ $W_xMo_{1-x}S_2$ keeping the lattice constant of WS_2 (Fig. S18 [49]). The results demonstrate that when x is 1, i.e., WS_2, it is topologically nontrivial with a band inversion. When x is decreased, the band inversion goes to disappear and becomes topologically trivial. $1H'$ $MoSe_2$ and WSe_2 monolayers exhibit topological transitions at the critical strain of 7% and 4%, respectively. The values of spin-orbit gaps for $1H'$ $MoSe_2$, WS_2, and WSe_2 are 18.7, 36.8, and 41.5 meV at the Dirac semimetal state. $1H'$ $MoTe_2$ and WTe_2 monolayers might make it hard to realize the topological transition under tensile strains due to the large energy gaps at the Γ point. The rich phase diagrams for $MoSe_2$, $MoTe_2$, WS_2, WSe_2, and WTe_2 are summarized in Fig. 5. As all these TMDs are structurally similar with different electronic structures, it could be highly possible to construct hybrid heterostructures with tuneable electronic functionality.

IV. CONCLUSION

In conclusion, we predicted a $1H'$ phase for MoS_2 monolayer and its family. Under a moderate external strain, these TMD monolayers present a rich phase diagram, including topologically trivial insulator states, 2D type-II Dirac semimetal states, and 2D ideal Dirac semimetal states protected by the coexistence of P and T symmetries. Topological edge states arise with gapless Dirac points, but possess a large effective mass that suggests potential applications in the study of strongly correlated states. Our work may pave the way for the future exploration of novel symmetry-protected Dirac states in TMD materials.

ACKNOWLEDGMENTS

The authors acknowledge funding support from the National Natural Science Foundation of China (Grants No. 11774127, No. 11822404, No. 11904142, No. 11722433, and No. 11674165), the Fok Ying-Tong Education Foundation of China (No. 161006), and the Fundamental Research Funds for the Central Universities (Grant No. 021314380147). The calculations were performed in the high-performance computing center of Jilin University, School of Physics and Electronic Engineering of Jiangsu Normal University and Nanjing University.

The authors declare no competing financial interest.

M.X. and G.Z. contributed equally to this work.

[1] N. P. Armitage, E. J. Mele, and A. Vishwanath, Rev. Mod. Phys. **90**, 015001 (2018).

[2] B. Yan and C. Felser, Annu. Rev. Condens. Matter Phys. **8**, 337 (2017).

[3] X. Wan, A. M. Turner, A. Vishwanath, and S. Y. Savrasov, Phys. Rev. B **83**, 205101 (2011).

[4] S.-Y. Xu, I. Belopolski, N. Alidoust, M. Neupane, G. Bian, C. Zhang, R. Sankar, G. Chang, Z. Yuan, C.-C. Lee, S.-M. Huang,

H. Zheng, J. Ma, D. S. Sanchez, B. Wang, A. Bansil, F. Chou, P. P. Shibayev, H. Lin, S. Jia, and M. Z. Hasan, Science **349**, 613 (2015).

[5] H. Weng, C. Fang, Z. Fang, B. A. Bernevig, and X. Dai, Phys. Rev. X **5**, 011029 (2015).

[6] S.-M. Huang, S.-Y. Xu, I. Belopolski, C.-C. Lee, G. Chang, B. Wang, N. Alidoust, G. Bian, M. Neupane, C. Zhang, S. Jia, A. Bansil, H. Lin, and M. Z. Hasan, Nat. Commun. **6**, 7373 (2015).

[7] X. Huang, L. Zhao, Y. Long, P. Wang, D. Chen, Z. Yang, H. Liang, M. Xue, H. Weng, Z. Fang, X. Dai, and G. Chen, Phys. Rev. X **5**, 031023 (2015).

[8] B. Q. Lv, N. Xu, H. M. Weng, J. Z. Ma, P. Richard, X. C. Huang, L. X. Zhao, G. F. Chen, C. E. Matt, F. Bisti, V. N. Strocov, J. Mesot, Z. Fang, X. Dai, T. Qian, M. Shi, and H. Ding, Nat. Phys. **11**, 724 (2015).

[9] L. X. Yang, Z. K. Liu, Y. Sun, H. Peng, H. F. Yang, T. Zhang, B. Zhou, Y. Zhang, Y. F. Guo, M. Rahn, D. Prabhakaran, Z. Hussain, S.-K. Mo, C. Felser, B. Yan, and Y. L. Chen, Nat. Phys. **11**, 728 (2015).

[10] A. A. Soluyanov, D. Gresch, Z. Wang, Q. Wu, M. Troyer, X. Dai, and B. A. Bernevig, Nature (London) **527**, 495 (2015).

[11] K. Deng, G. Wan, P. Deng, K. Zhang, S. Ding, E. Wang, M. Yan, H. Huang, H. Zhang, Z. Xu, J. Denlinger, A. Fedorov, H. Yang, W. Duan, H. Yao, Y. Wu, S. Fan, H. Zhang, X. Chen, and S. Zhou, Nat. Phys. **12**, 1105 (2016).

[12] J. Jiang, Z. K. Liu, Y. Sun, H. F. Yang, C. R. Rajamathi, Y. P. Qi, L. X. Yang, C. Chen, H. Peng, C.-C. Hwang, S. Z. Sun, S.-K. Mo, I. Vobornik, J. Fujii, S. S. P. Parkin, C. Felser, B. H. Yan, and Y. L. Chen, Nat. Commun. **8**, 13973 (2017).

[13] J. Ruan, S.-K. Jian, H. Yao, H. Zhang, S.-C. Zhang, and D. Xing, Nat. Commun. **7**, 11136 (2016).

[14] J. Ruan, S.-K. Jian, D. Zhang, H. Yao, H. Zhang, S.-C. Zhang, and D. Xing, Phys. Rev. Lett. **116**, 226801 (2016).

[15] Z. Wang, Y. Sun, X.-Q. Chen, C. Franchini, G. Xu, H. Weng, X. Dai, and Z. Fang, Phys. Rev. B **85**, 195320 (2012).

[16] Z. Wang, H. Weng, Q. Wu, X. Dai, and Z. Fang, Phys. Rev. B **88**, 125427 (2013).

[17] S. Borisenko, Q. Gibson, D. Evtushinsky, V. Zabolotnyy, B. Büchner, and R. J. Cava, Phys. Rev. Lett. **113**, 027603 (2014).

[18] Z. K. Liu, B. Zhou, Y. Zhang, Z. J. Wang, H. M. Weng, D. Prabhakaran, S.-K. Mo, Z. X. Shen, Z. Fang, X. Dai, Z. Hussain, and Y. L. Chen, Science **343**, 864 (2014).

[19] B. Q. Lv, Z.-L. Feng, Q.-N. Xu, X. Gao, J.-Z. Ma, L.-Y. Kong, P. Richard, Y.-B. Huang, V. N. Strocov, C. Fang, H.-M. Weng, Y.-G. Shi, T. Qian, and H. Ding, Nature (London) **546**, 627 (2017).

[20] J. Xiong, S. K. Kushwaha, T. Liang, J. W. Krizan, M. Hirschberger, W. Wang, R. J. Cava, and N. P. Ong, Science **350**, 413 (2015).

[21] Z. K. Liu, J. Jiang, B. Zhou, Z. J. Wang, Y. Zhang, H. M. Weng, D. Prabhakaran, S.-K. Mo, H. Peng, P. Dudin, T. Kim, M. Hoesch, Z. Fang, X. Dai, Z. X. Shen, D. L. Feng, Z. Hussain, and Y. L. Chen, Nat. Mater. **13**, 677 (2014).

[22] B. Q. Lv, S. Muff, T. Qian, Z. D. Song, S. M. Nie, N. Xu, P. Richard, C. E. Matt, N. C. Plumb, L. X. Zhao, G. F. Chen, Z. Fang, X. Dai, J. H. Dil, J. Mesot, M. Shi, H. M. Weng, and H. Ding, Phys. Rev. Lett. **115**, 217601 (2015).

[23] Y. Sun, S.-C. Wu, and B. Yan, Phys. Rev. B **92**, 115428 (2015).

[24] M. Z. Hasan, S.-Y. Xu, I. Belopolski, and S.-M. Huang, Annu. Rev. Condens. Matter Phys. **8**, 289 (2017).

[25] H. Li, H. He, H.-Z. Lu, H. Zhang, H. Liu, R. Ma, Z. Fan, S.-Q. Shen, and J. Wang, Nat. Commun. **7**, 10301 (2016).

[26] M. Hirata, K. Ishikawa, G. Matsuno, A. Kobayashi, K. Miyagawa, M. Tamura, C. Berthier, and K. Kanoda, Science **358**, 1403 (2017).

[27] S. V. Ramankutty, J. Henke, A. Schiphorst, R. Nutakki, S. Bron, G. Araizi-Kanoutas, S. Mishra, L. Li, Y. Huang, T. Kim, M. Hoesch, C. Schlueter, T.-L. Lee, A. de Visser, Z. Zhong, J. van Wezel, E. van Heumen, and M. Golden, SciPost Phys. **4**, 010 (2018).

[28] S. M. Young and C. L. Kane, Phys. Rev. Lett. **115**, 126803 (2015).

[29] C.-C. Liu, W. Feng, and Y. Yao, Phys. Rev. Lett. **107**, 076802 (2011).

[30] Y. Xu, B. Yan, H.-J. Zhang, J. Wang, G. Xu, P. Tang, W. Duan, and S.-C. Zhang, Phys. Rev. Lett. **111**, 136804 (2013).

[31] M. E. Dávila, L. Xian, S. Cahangirov, A. Rubio, and G. Le Lay, New J. Phys. **16**, 095002 (2014).

[32] M. Ezawa, J. Phys. Soc. Jpn. **84**, 121003 (2015).

[33] L. Li, Y. Yu, G. J. Ye, Q. Ge, X. Ou, H. Wu, D. Feng, X. H. Chen, and Y. Zhang, Nat. Nanotechnol. **9**, 372 (2014).

[34] Q. H. Wang, K. Kalantar-Zadeh, A. Kis, J. N. Coleman, and M. S. Strano, Nat. Nanotechnol. **7**, 699 (2012).

[35] X. Qian, J. Liu, L. Fu, and J. Li, Science **346**, 1344 (2014).

[36] Z. Wang, D. Gresch, A. A. Soluyanov, W. Xie, S. Kushwaha, X. Dai, M. Troyer, R. J. Cava, and B. A. Bernevig, Phys. Rev. Lett. **117**, 056805 (2016).

[37] Y. Sun, S.C. Wu, M. N. Ali, C. Felser, and B. Yan, Phys. Rev. B **92**, 161107(R) (2015).

[38] Y. Wang, J. Lv, L. Zhu, and Y. Ma, Comput. Phys. Commun. **183**, 2063 (2012).

[39] Y. Wang, J. Lv, L. Zhu, and Y. Ma, Phys. Rev. B **82**, 094116 (2010).

[40] W. Kohn and L. J. Sham, Phys. Rev. **140**, A1133 (1965).

[41] G. Kresse, J. Non-Cryst. Solids **192-193**, 222 (1995).

[42] P. E. Blöchl, Phys. Rev. B **50**, 17953 (1994).

[43] J. P. Perdew, K. Burke, and M. Ernzerhof, Phys. Rev. Lett. **77**, 3865 (1996).

[44] H. J. Monkhorst and J. D. Pack, Phys. Rev. B **13**, 5188 (1976).

[45] K. Parlinski, Z. Q. Li, and Y. Kawazoe, Phys. Rev. Lett. **78**, 4063 (1997).

[46] A. Togo, F. Oba, and I. Tanaka, Phys. Rev. B **78**, 134106 (2008).

[47] J. Heyd, G. E. Scuseria, and M. Ernzerhof, J. Chem. Phys. **118**, 8207 (2003).

[48] H.-J. Zhang, C.-X. Liu, X.-L. Qi, X.-Y. Deng, X. Dai, S.-C. Zhang, and Z. Fang, Phys. Rev. B **80**, 085307 (2009).

[49] See Supplemental Material at http://link.aps.org/supplemental/10.1103/PhysRevB.100.235435 for POSCAR files of $1H'$ MoS_2 monolayer; phonon band dispersions and the AIMD simulations results; lattice parameters and band structures using PBEsol functionals; the effect of uniaxial strain on topological states; edge states; the projected band structures of $1H'$ MoS_2 without and with SOC; phonon band dispersions of $1H'$ $MoSe_2$, $1H'$ $MoTe_2$, $1H'$ WS_2, $1H'$ WSe_2, and $1H'$ WTe_2; band structures of $1H'$ $MoSe_2$, $1H'$-$MoTe_2$,

$1H'$ WS_2, $1H'$ WSe_2, and $1H'$ WTe_2 in PBE level under different biaxial strains; and band structures of $1H'$ $W_xMo_{1-x}S_2$.

[50] F. Ma, G. Gao, Y. Jiao, Y. Gu, A. Bilic, H. Zhang, Z. Chen, and A. Du, Nanoscale **8**, 4969 (2016).

[51] E. Tang and L. Fu, Nat. Phys. **10**, 964 (2014).

[52] E. Taghizadeh Sisakht, F. Fazileh, M. H. Zare, M. Zarenia, and F. M. Peeters, Phys. Rev. B **94**, 085417 (2016).

[53] C. Chen, S.-S. Wang, L. Liu, Z.-M. Yu, X.-L. Sheng, Z. Chen, and S. A. Yang, Phys. Rev. Mater. **1**, 044201 (2017).

[54] M. Yan, H. Huang, K. Zhang, E. Wang, W. Yao, K. Deng, G. Wan, H. Zhang, M. Arita, H. Yang, Z. Sun, H. Yao, Y. Wu, S. Fan, W. Duan, and S. Zhou, Nat. Commun. **8**, 257 (2017).

[55] T.-R. Chang, S.-Y. Xu, D. S. Sanchez, W.-F. Tsai, S.-M. Huang, G. Chang, C.-H. Hsu, G. Bian, I. Belopolski, Z.-M. Yu, S. A. Yang, T. Neupert, H.-T. Jeng, H. Lin, and M. Z. Hasan, Phys. Rev. Lett. **119**, 026404 (2017).

[56] H. Weng, Y. Liang, Q. Xu, R. Yu, Z. Fang, X. Dai, and Y. Kawazoe, Phys. Rev. B **92**, 045108 (2015).

[57] K. Zollner, P. E. Faria Junior, and J. Fabian, Phys. Rev. B **100**, 195126 (2019).

[58] Y. Kang, S. Najmaei, Z. Liu, Y. Bao, Y. Wang, X. Zhu, N. J. Halas, P. Nordlander, P. M. Ajayan, J. Lou, and Z. Fang, Adv. Mater. **26**, 6467 (2014).

[59] B. Radisavljevic and A. Kis, Nat. Mater. **12**, 815 (2013).